biomedicines

MDPI

Article

Linea Alba Interstitium as a Tunable Corridor for Gold Nanoparticle Delivery: Distinct Biodistribution from Intravenous Administration

Yu Jin [1,2,†], Yujiao Sun [3,4,†], Weibo Zhang [1], Yajing A [1,5], Jianjie Luo [1], Yifan Li [3,4], Shuyou Wang [1], Shuyong Jia [1], Guangjun Wang [1], Simin Zhao [1], Rongcheng Han [3,4,*] and Xiaojing Song [1,*]

[1] Department of Biomedical Engineering, Institute of Acupuncture and Moxibustion, China Academy of Chinese Medical Sciences, Beijing 100700, China; jy_1232026@163.com (Y.J.); a12320242024@163.com (Y.A.); luojianjie064@163.com (J.L.); wangsy15@126.com (S.W.); shuyong6666@163.com (S.J.); cacms_guangjun@163.com (G.W.); zhaosimin123123@163.com (S.Z.)
[2] School of Acupuncture-Moxibustion and Tuina, Tianjin University of Traditional Chinese Medicine, Tianjin 301617, China
[3] Laboratory of Integrative Physiology, Institute of Genetics and Developmental Biology, Chinese Academy of Sciences, Beijing 100101, China; yj.sun@genetics.ac.cn (Y.S.); yifanli1007@genetics.ac.cn (Y.L.)
[4] College of Advanced Agricultural Sciences, University of Chinese Academy of Sciences, Beijing 101408, China
[5] Department of Traditional Chinese Medicine, Qinghai University Medical College, Qinghai University, Xining 810016, China
* Correspondence: hanrch@genetics.ac.cn (R.H.); songxiaojing@mail.cintcm.ac.cn (X.S.)
† These authors contributed equally to this study.

Abstract

Background: Achieving efficient extravascular nanoparticle delivery to deep viscera is hindered by rapid reticuloendothelial clearance and multiple biological barriers. We explored whether the linea alba (LA) interstitium acts as a route for gold nanoparticle (AuNP) delivery. **Methods:** PEGylated 20 nm AuNPs were interstitially injected into the rat LA under anesthetized, awake, electroacupuncture (EA), and moxibustion (Moxi) conditions; paramedian muscle and tail vein injections served as controls. **Results:** Micro-CT and ICP-MS showed that LA injection supported directional AuNP migration along the midline, with relatively high normalized concentration-based index values for the ovaries (23.04%) and bladder (20.22%). By comparison, intravenous injection was associated with higher normalized values in the liver, spleen, and lungs. The awake state promoted systemic entry of Au and splenic accumulation; EA increased Au distribution within the uterus; and Moxi boosted systemic transport. Histology identified a loose reticular collagen network with expanded interstitial spaces within the LA. **Conclusions:** These findings suggest that the LA interstitium is a promising interstitial nano-delivery pathway, where nanoparticle biodistribution can be tuned by physiological status and physical stimuli.

Keywords: nanoparticles; gold nanoparticles; linea alba; interstitium; drug delivery

Academic Editor: Ilaria Ottonelli

Received: 7 September 2026
Revised: 28 October 2026
Accepted: 30 October 2026
Published: 3 November 2026

Copyright: © 2026 by the authors. Licensee MDPI, Basel, Switzerland. This article is an open access article distributed under the terms and conditions of the Creative Commons Attribution (CC BY) license.

1. Introduction

Can interstitial administration of nanoparticles into the linea alba (LA) produce distinct migration and biodistribution patterns compared with intravenous

administration routes? Here, we hypothesized that the LA interstitium may support long-range nanoparticle migration through its intrinsic anatomical connectivity and exhibit a distinct organ distribution profile. We further hypothesized that LA-mediated transport can be modulated by physiological state and external physical stimuli. To test these hypotheses, we employed PEGylated gold nanoparticles (AuNPs, ~20 nm) as traceable probes and combined Micro-CT imaging for real-time migration tracking with Inductively Coupled Plasma-Mass Spectrometry (ICP-MS) for quantitative biodistribution analysis across major organs.

Nanoparticle-based drug delivery systems have garnered substantial attention over the past two decades owing to their tunable physicochemical properties, high drug-loading capacity, and potential for controlled release [1]. To date, the vast majority of nanomedicine administration strategies rely on the vascular route, with intravenous injection being the most extensively investigated, which allows nanoparticles to directly enter the systemic circulation and achieve whole-body distribution [2]. However, this vascular-dependent paradigm has inherent limitations. Once in the bloodstream, nanoparticles are rapidly opsonized by plasma proteins to form a "protein corona," which alters their biological identity and often triggers accelerated clearance by the reticuloendothelial system [3–5]. Consequently, systemically administered nanoparticles tend to accumulate predominantly in the liver, spleen, and lungs, whereas their distribution to extrahepatic organs, particularly deep-seated pelvic organs such as the bladder, uterus, and ovaries, may be limited [6,7]. Despite extensive efforts in surface engineering, including PEGylation, ligand conjugation, and biomimetic coating, to prolong circulation time and improve tissue distribution, efficient extravascular delivery to pelvic tissues remains challenging [8,9]. These limitations underscore the need to explore delivery routes that complement the conventional vascular system.

The interstitial space, which constitutes the microenvironment that nanoparticles encounter immediately after extravasation, has recently attracted increasing attention as a critical determinant of nanoparticle transport and distribution [10]. In solid tumors, extensive research has demonstrated that nanoparticle penetration is severely hindered by aberrant extracellular matrix remodeling, collagen densification, elevated interstitial fluid pressure, and abnormal microvasculature, collectively forming formidable transport barriers [11,12]. However, outside the pathological tumor context, normal tissues also possess structured interstitial networks that may support fluid and particulate transport within specific anatomical regions [13–18]. The landmark discovery by Benias et al. [19] of a previously unrecognized, fluid-filled interstitial space network in human tissues challenged the traditional view of the interstitium as merely a passive supporting structure and suggested that it may function as a dynamic communication pathway. This raises an intriguing possibility: can naturally occurring interstitial structures support the migration of nanoparticles over anatomically extended distances and contribute to distribution patterns that differ from those following conventional vascular administration?

The LA, a tendinous structure formed by the interweaving of aponeuroses of the abdominal wall muscles along the ventral midline—presents a particularly interesting candidate in this context. Unlike adjacent paramuscular connective tissue, the LA is characterized by a distinctive collagen fiber arrangement with longitudinally oriented, loosely organized reticular networks and enlarged interstitial spaces, as revealed by recent histomorphological studies [20]. Functionally, previous studies have reported low-hydraulic-resistance pathways in the LA that support longitudinal tracer migration along the midline [20]. Subsequent studies demonstrated that interstitial fluid transport within the LA participates in acupuncture-induced remote tissue regulation and that administration of exogenous substances into this region can be associated with their

distribution to pelvic organs [21,22]. Notably, these findings have been primarily obtained using small-molecule dyes and fluidic tracers, leaving a critical question unanswered: can nanoparticles of nanoscale dimensions migrate following LA interstitial administration, and does this administration route produce a biodistribution profile distinguishable from that observed following vascular administration?

In the present study, in addition to characterizing the migration characteristics associated with LA interstitial administration, we explored two biologically and translationally relevant modulatory dimensions: (i) the influence of physiological state (anesthetized resting vs. awake ambulatory status) and (ii) the impact of external physical stimuli-specifically electroacupuncture and moxibustion-which represent clinically utilized interventions known to affect interstitial fluid dynamics and local tissue perfusion [3,23]. By systematically examining these variables, we aimed to characterize nanoparticle migration and biodistribution following LA interstitial administration, compare distribution patterns with those following intravenous administration, and assess their modulation by physiological state and physical stimulation.

The findings of this study provide proof-of-concept evidence that LA interstitial administration of AuNPs is associated with distinct migration characteristics and biodistribution patterns, and that these patterns vary with physiological state and external physical stimulation. Although the observed findings suggest that the LA interstitium may be a useful anatomical site for exploring alternative approaches to nanoparticle administration, the relative contributions of interstitial transport, lymphatic drainage, and entry into the systemic circulation remain to be clarified. This study expands our understanding of nanoparticle distribution following interstitial administration and provides a basis for further investigating the potential of anatomically guided interstitial delivery, particularly for applications involving pelvic organs.

2. Materials and Methods

2.1. Preparation of AuNPs

Chloroauric acid tetrahydrate ($HAuCl_4 \cdot 4\ H_2O$, CAS NO. 10010711) and citrate (CAS NO. 77-92-9) were purchased from Macklin Inc. (Shanghai, China). Mercapto polyethylene glycol was obtained from Aladdin (Shanghai, China). All reagents were used as received without further purification.

AuNPs were synthesized via citrate reduction in $HAuCl_4$ according to a previously described procedure [24]. All glassware was thoroughly cleaned before use. An aqueous solution of $HAuCl_4$ (1 mM, 50 mL) was brought to a vigorous reflux under magnetic stirring. A predetermined volume of sodium citrate solution was quickly added in one portion. The reaction was refluxed for 15 min until a stable wine-red color developed. UV–Vis absorption spectra were recorded using a UV1901PC spectrophotometer (Shanghai AuCy Scientific Instrument Co., Ltd., Shanghai, China) over a wavelength range of 200–800 nm at room temperature using a quartz cuvette, with a surface plasmon resonance (SPR) absorption peak appearing at approximately 520 nm, indicating completion of the reduction reaction. To reduce nanoparticle aggregation and improve colloidal stability during storage, the AuNPs were subsequently modified with mPEG-SH (0.1 mM). The morphology and core diameter of the AuNPs were characterized using a Talos L120C G2 transmission electron microscope (Thermo Fisher Scientific Inc., Waltham, MA, USA) operated at an accelerating voltage of 120 kV.

The hydrodynamic diameter and zeta potential of the AuNPs were measured using a Malvern Zetasizer Nano ZS90 (Malvern Panalytical Ltd., Malvern, Worcestershire, UK). Approximately 1 mL of AuNP suspension was collected and sonicated for 5 min before measurement. The sample was then slowly transferred into the measurement cuvette to avoid bubble formation. The instrument was preheated for 30 min before measurement.

Measurements were performed at 25 °C after a 30 s equilibration period using the corresponding measurement programs for hydrodynamic diameter and zeta potential. At each time point, the same AuNP suspension was measured three times as technical replicates. The same suspension was monitored for 6 days, with results expressed as mean ± SD of three technical replicates at each time point.

2.2. Animals

Forty-eight specific pathogen-free female Sprague–Dawley rats, aged 7–8 weeks, were obtained from Beijing Vital River Laboratory Animal Technology Co., Ltd. (Beijing, China). Animals were housed individually in cages within the animal facility of the Institute of Acupuncture and Moxibustion, China Academy of Chinese Medical Sciences (clean-grade environment). The facility was maintained at (20 ± 2) °C with a relative humidity of (55 ± 4)%, under a 12 h light/dark cycle (lights on: 8:00–20:00; lights off: 20:00–8:00) with adequate ventilation. Rats had ad libitum access to standard chow and purified water and were acclimatized for 1 week prior to experimentation. All animal procedures were performed in accordance with the Regulations of the Medical Experimental Animal Center of the China Academy of Chinese Medical Sciences. The experimental protocol was approved by the Animal Ethics Committee of the Institute of Acupuncture and Moxibustion (Approval No. D2023-01-10-01; Date: 10 January 2023). The rats were randomly assigned into six experimental groups, each comprising eight animals: the anesthesia group (Anesthesia), electroacupuncture group (EA), moxibustion group (Moxi), awake group (Awake), and paramedian injection control group (Ctrl), and intravenous injection group(i.v.) (*n* = 8). Following grouping, the corresponding experimental procedures were performed as described below.

2.3. Experimental Design and Intervention Procedures

After abdominal depilation, rats in the Anesthesia, EA, Moxi, and Awake groups received an interstitial injection of AuNPs (25 μL, 10 mg/mL, 20 nm) into the LA under inhalation anesthesia. The injection site was located at the 2/5 point from the xiphoid process toward the pubic symphysis along the linea alba, with an injection depth of approximately 2 mm. All injections were performed by the same operator using a 0.45 mm diameter needle connected to a microinjection pump, with an injection volume of 25 μL over approximately 3 min. Subsequently, different conditions were applied for 20 min: the Anesthesia group was maintained under anesthesia without additional stimulation; the EA group received continuous-wave electroacupuncture stimulation (2 Hz); the Moxi group received thermal stimulation using a lit incense stick positioned approximately 0.5–1 cm above the injection site; and the Awake group was returned to the cage for unrestricted activity. The Ctrl group received an equivalent dose of AuNPs injected into the adjacent paramedian muscle layer at the same depth under inhalation anesthesia, and all injections were performed by the same operator using a unified procedure. Additionally, a separate i.v. group was included. AuNPs (30 μL, 10 mg/mL, 20 nm) were administered intravenously. The i.v. volume was slightly increased from 25 μL to 30 μL to compensate for potential injection-related residuals in the tail associated with the slow, low-pressure pump infusion, thereby reducing variability in the amount delivered into the body.

After completion of the experimental procedures, blood samples (100 μL) and major organs, including the heart, liver, spleen, lungs, kidneys, uterus, ovaries, bladder, and intestine, were collected. The wet weights of the collected organs were recorded, and approximately 200 mg of each tissue sample was transferred into 15 mL centrifuge tubes and stored at −20 °C for subsequent ICP-MS analysis. Abdominal wall tissues containing

the injection region were collected and stored at 4 °C for Micro-CT imaging analysis (Figure 1).

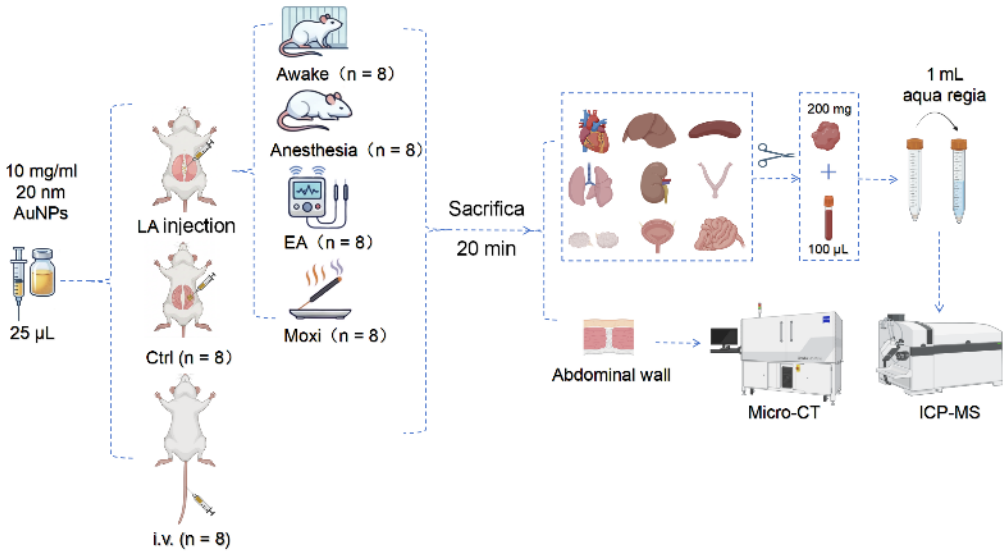


Figure 1. Experimental design for evaluating AuNP transport and biodistribution after LA injection.

2.4. Micro-CT Imaging and Image Analysis

To visualize the three-dimensional distribution and migration characteristics of gold nanoparticles (AuNPs) within the linea alba and surrounding tissues, Micro-CT imaging was performed using a Zeiss Micro-CT 100 system (Zeiss Microscopy GmbH, Jena, Germany). Samples were scanned at an X-ray energy of 45 kVp and a tube current of 88 μA (4 W), with a spatial resolution of 10 μm. The scanning field of view was set to a diameter of 9 mm and a height of 78 mm, and a total of 260 tomographic slices were acquired for each sample. The reconstructed three-dimensional datasets were generated using the manufacturer's reconstruction software. The spatial distribution patterns and migration trajectories of AuNPs within tissues were subsequently visualized and analyzed based on the reconstructed Micro-CT images. For quantitative Micro-CT analysis, one sample per group was excluded because the AuNP signal in the region of interest could not be clearly identified, preventing migration trajectory measurement, resulting in a final sample size of $n = 7$ per group.

2.5. Quantification of Au Content in Tissues by ICP-MS

Tissue and blood samples were collected for quantitative determination of Au biodistribution. Approximately 200 mg of each tissue sample or 100 μL of blood was transferred into digestion tubes, followed by the addition of 1 mL aqua regia composed of concentrated nitric acid (HNO_3, 69–71%; Kermel, Tianjin, China) and hydrochloric acid (HCl, 36–38%; Kermel, Tianjin, China) at a volume ratio of 1:3 (*v*/*v*). Samples were digested in a thermostatic drying oven at 120 °C for approximately 30 min. After cooling, the digested solutions were transferred, diluted to a constant volume with ultrapure water, and subjected to gold-content quantification via an inductively coupled plasma mass spectrometer (NexION 300D ICP-MS; PerkinElmer, Inc., Waltham, MA, USA).The instrument was operated under the following conditions: RF power of 1550 W, plasma gas flow rate of 18 L/min, auxiliary gas flow rate of 1.2 L/min, and nebulizer gas flow rate of 1.08 L/min. Au concentrations were determined using calibration curves generated from Au standard solutions. The percentage of injected dose per gram of tissue (%ID/g) was calculated as $C/D_{total} \times 100\%$, where C represents the Au content measured by ICP-

MS in each tissue sample (μg Au/g tissue), and D_{total} represents the total amount of Au administered in a single injection (μg). To compare the relative Au enrichment among different organs, the normalized concentration-based index for each organ was calculated as its %ID/g divided by the summed %ID/g values of all analyzed organs, which was defined as 100%. Each sample was measured three times as technical replicates, and the mean of the three measurements was used for subsequent statistical analysis.

2.6. Immunofluorescence Staining of the LA

Following transcardial perfusion, abdominal wall tissue blocks (1 × 1 cm, n = 3) containing the LA and adjacent paramedian abdominal wall tissue were collected from the same experimental cohort and post-fixed in 4% paraformaldehyde (PFA) at 4 °C for 4–6 h. The tissues were embedded in optimal cutting temperature (OCT) compound and cryosectioned at 20 μm in horizontal and vertical orientations. The sections were permeabilized with 0.5% Triton X-100 for 20 min and blocked with 10% donkey serum for 1 h at room temperature. The sections were then incubated overnight at 4 °C with primary antibodies against COL-I (NB600-450, Novus Biologicals, Centennial, CO, USA, 1:1000), LYVE-1 (67538S, Cell Signaling Technology, Inc., Danvers, MA, USA, 1:400), and CD31 (AF3628, R&D Systems, Inc. (Bio-Techne), Minneapolis, MN, USA, 1:60). After three washes with phosphate-buffered saline (PBS), the sections were incubated with the corresponding fluorophore-conjugated secondary antibodies for 1 h at room temperature in the dark. Following additional PBS washes, the sections were mounted using a DAPI-containing mounting medium. Fluorescence images were acquired using a Nikon AX high-resolution spectral imaging platform.

2.7. Masson Trichrome Staining of the LA

Abdominal wall tissue blocks (1 × 1 cm) containing the LA and adjacent paramedian connective tissue were collected from three rats (n = 3) from the same experimental cohort and fixed in 4% paraformaldehyde (PFA) at 4 °C for 48 h. The tissues were dehydrated through a graded ethanol series, cleared in xylene, paraffin-embedded, and sectioned at 10 μm. Sections oriented parallel (horizontal sections) or perpendicular (vertical sections) to the abdominal wall were subjected to Masson trichrome staining. After deparaffinization and rehydration, the sections were incubated in Bouin's solution preheated to 60 °C for 1 h to enhance staining intensity. The sections were then sequentially stained with Weigert's iron hematoxylin, Biebrich scarlet–acid fuchsin, phosphotungstic–phosphomolybdic acid, and aniline blue according to the standard protocol. After differentiation with 1% acetic acid, the sections were dehydrated, cleared, and mounted using a resinous mounting medium. Images were acquired using a light microscope.

2.8. Statistical Analysis

Statistical analyses and graphical presentations were performed using GraphPad Prism software (Version 10.1.2; GraphPad Software, San Diego, CA, USA). Data are presented as mean ± standard deviation (SD). Data distribution was assessed using the Shapiro–Wilk normality test. Comparisons between two groups were performed using unpaired two-tailed Student's t-tests. Multiple-group comparisons were conducted using one-way ANOVA, followed by Tukey's post hoc test. For comparisons across multiple organs, a mixed-effects model was used, with treatment group and organ included as fixed effects and animal identity as a random effect to account for within-animal correlations among organ measurements. Tukey's multiple-comparison test was used for post hoc comparisons, and adjusted p values were reported. The p value < 0.05 was considered statistically significant.

3. Results

3.1. Synthesis and Characterization of AuNPs

AuNPs were prepared via citrate-mediated reduction in $HAuCl_4$ and subsequently stabilized with mPEG-SH (0.1 mM). UV–Vis spectroscopy revealed a surface plasmon resonance peak at approximately 520 nm (Figure 2A). Transmission electron microscopy (TEM) showed predominantly spherical nanoparticles (Figure 2B), with a mean core diameter of 19.04 ± 3.67 nm based on 100 particles (Figure 2C). TEM was used to determine the physical diameter of the gold core, whereas dynamic light scattering (DLS) was used to measure the hydrodynamic diameter in suspension. To monitor changes in the physicochemical properties over time, the hydrodynamic diameter, polydispersity index (PDI), and zeta potential of the same AuNP suspension were measured over 6 days (Figure 2D,E; Supplementary Table S1). The mean hydrodynamic diameter ranged from 33.89 to 34.29 nm, the mean PDI from 0.288 to 0.324, and the mean zeta potential from −16.6 to −15.5 mV. No marked changes in these mean values were observed during the monitoring period, indicating that the measured parameters of this suspension remained relatively consistent over 6 days.

PEGylated AuNPs were selected as tracer probes due to their high X-ray attenuation, enabling direct Micro-CT visualization of migration without additional labeling, and sensitive ICP-MS detection, allowing complementary evaluation of migration and tissue distribution. However, ICP-MS only quantifies the total elemental Au content and cannot differentiate intact nanoparticles from potentially transformed forms, such as protein-bound or ionic gold species; the results represent elemental Au distribution rather than confirmed intact nanoparticle accumulation. Moreover, the persistent nature of the gold core and the lack of therapeutic payloads limit conclusions regarding long-term clearance, safety, and therapeutic efficacy. Future studies should evaluate drug-loaded nanocarriers with diverse physicochemical properties and particle sizes.

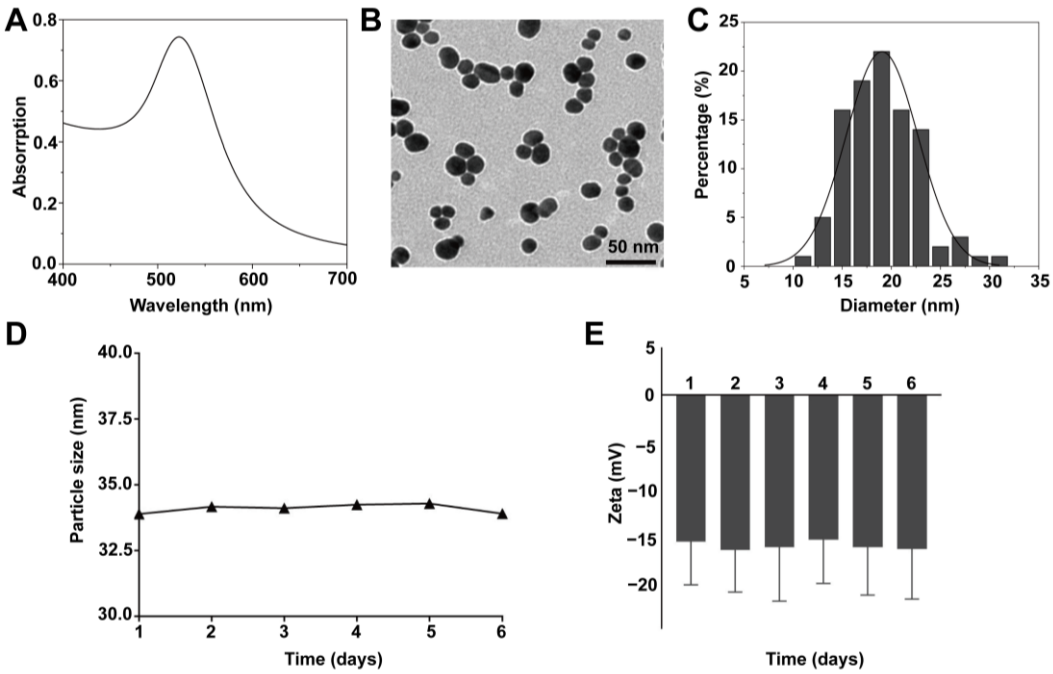


Figure 2. Characterization and stability of AuNPs. (**A**) UV–Vis absorption spectrum of AuNPs; (**B**) representative transmission electron microscopy (TEM) image, with a scale bar of 50 nm; (**C**) core size distribution of AuNPs, with an average diameter of 19.04 ± 3.67 nm; (**D**) changes in AuNP size (measured by DLS) and (**E**) changes in zeta potential over 6 days.

3.2. LA Interstitium Confers Distinct AuNP Migration Characteristics and Biodistribution Patterns

Micro-CT imaging revealed markedly different AuNP distribution profiles following injection into distinct anatomical sites (Figure 3A). In the Anesthesia group, AuNPs exhibited partial longitudinal extension along the LA interstitial region, accompanied by lateral diffusion into adjacent muscular tissues. In contrast, the Ctrl group (paramedian muscle injection) displayed radial diffusion centered at the injection site. Quantitative analysis showed no significant difference in AuNP migration trajectory length between the two groups (Figure 3B). ICP-MS analysis demonstrated that blood Au content in the Ctrl group was significantly higher than that in the Anesthesia group (* $p < 0.05$, Figure 3C). Further examination of Au distribution across major organs—including the heart, liver, spleen, lungs, kidneys, uterus, ovaries, bladder, and intestine—revealed that the Anesthesia group exhibited significantly elevated Au content in the kidneys (*** $p < 0.001$), ovaries (** $p < 0.001$), and bladder (** $p < 0.01$) compared with the Ctrl group (Figure 3D). Moreover, comparative analysis of Au distribution using a normalized concentration-based index following interstitial versus intravenous administration demonstrated distinct organ distribution profile (Figure 3E–G). In the interstitial injection group, the highest normalized concentration-based index values were observed in the ovaries (23.04%) and bladder (20.22%), whereas the intravenous group showed the highest index values in the spleen (36.76%), liver (18.20%), and lungs (15.03%). Collectively, these findings indicate that AuNPs exhibit fundamentally different migration behaviors and tissue distribution patterns following injection via the LA interstitium, paramedian muscle, or tail vein, suggesting that the LA interstitium may constitute a nano-delivery pathway distinct from the blood circulation route.

3.3. Physiological State Modulates AuNP Migration and Biodistribution via the LA Interstitium

To investigate the regulatory effect of physiological state on nanoparticle transport through the LA interstitium, we compared AuNP migration characteristics and tissue distribution between anesthetized and awake states (Figure 4). Micro-CT imaging revealed distinct migration behaviors of AuNPs between the two groups (Figure 4A). Compared with the Anesthesia group, the Awake group exhibited a broader longitudinal distribution of AuNPs along the LA interstitium. Quantitative analysis demonstrated that the AuNP migration trajectory length in the Awake group was significantly increased relative to that in the Anesthesia group (*** $p < 0.001$, Figure 4B). ICP-MS analysis showed that blood Au content in the Awake group was significantly higher than that in the Anesthesia group (*** $p < 0.001$, Figure 4C). Further examination of Au content in major organs—including the heart, liver, spleen, lungs, kidneys, uterus, ovaries, bladder, and intestine—revealed that the Awake group exhibited significantly elevated gold accumulation in the spleen compared with the Anesthesia group (*** $p < 0.001$, Figure 4D). Collectively, these results suggest that, following LA interstitial injection, the awake state is accompanied by a systemic distribution pattern, characterized by elevated blood Au levels and increased splenic accumulation.

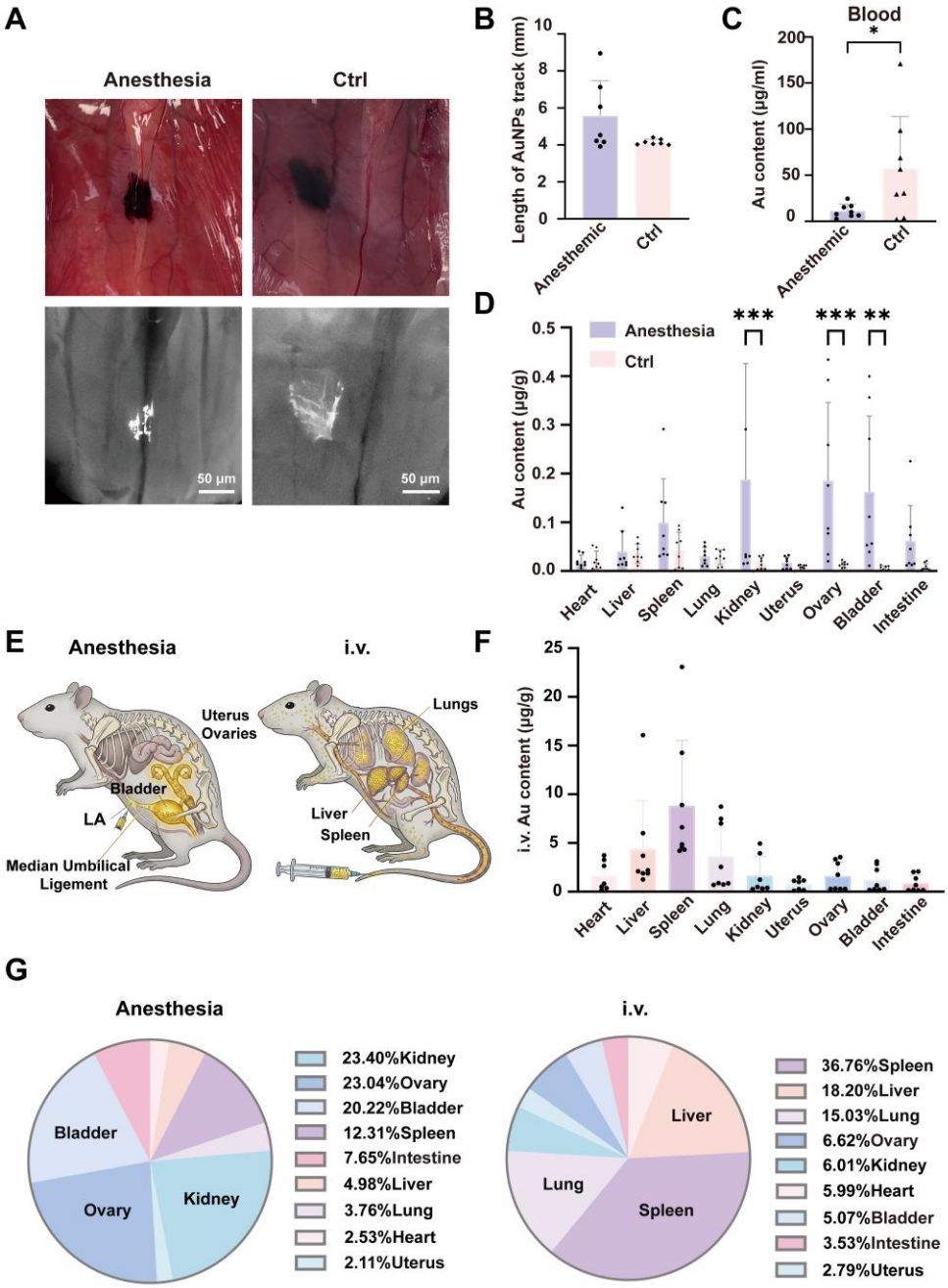


Figure 3. AuNP migration and biodistribution. (**A**) Micro-CT images of AuNP migration, Anesthesia vs. Ctrl, Scale bar: 50 μm; (**B**) migration length of AuNPs, Anesthesia vs. Ctrl ($n = 7$); (**C**) blood Au content detected by ICP-MS, Anesthesia vs. Ctrl ($n = 8$); (**D**) organ Au distribution detected by ICP-MS, Anesthesia vs. Ctrl ($n = 8$); (**E**) schematic illustration of AuNPs administration routes, Anesthesia vs. i.v.; (**F**) organ distribution of Au after tail vein injection ($n = 8$); (**G**) normalized concentration-based index of Au (%), Anesthesia vs. i.v. ($n = 8$). (*) means $p < 0.05$; (**) means $p < 0.01$; (***) means $p < 0.001$.

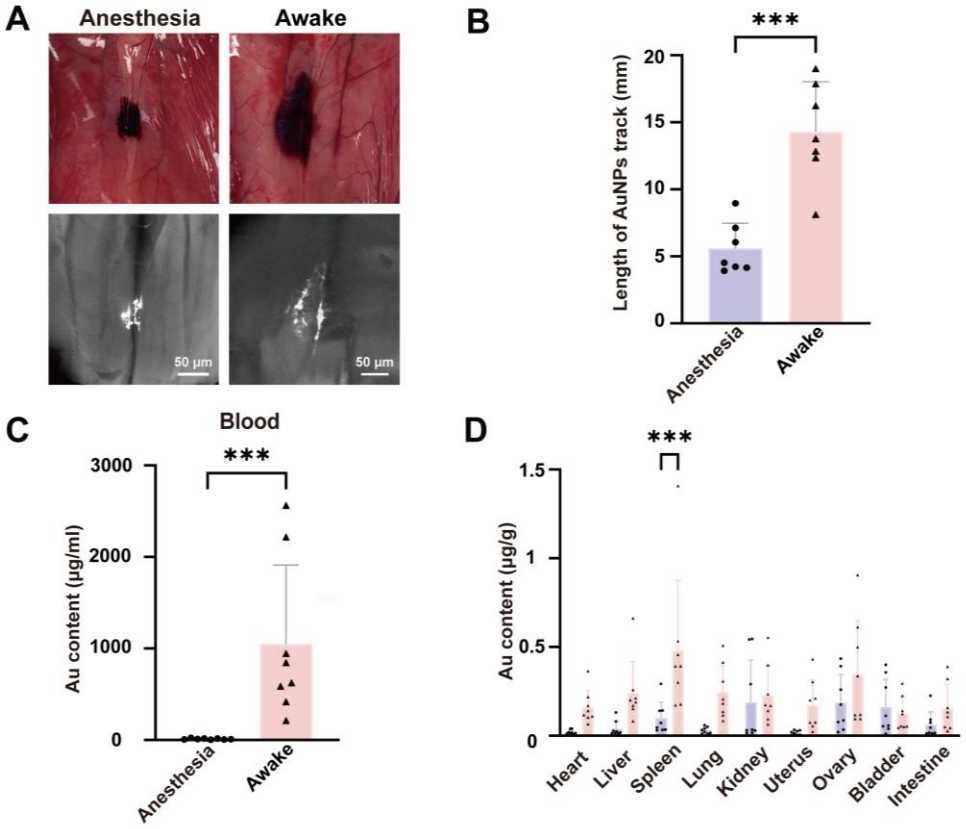


Figure 4. Physiological state regulates AuNP transport and distribution. (**A**) Micro-CT images of AuNP migration, Anesthesia vs. Awake, Scale bar: 50 μm; (**B**) migration length of AuNPs, Anesthesia vs. Awake (n = 7); (**C**) blood Au content detected by ICP-MS, Anesthesia vs. Awake (n = 8); (**D**) organ Au distribution detected by ICP-MS, Anesthesia vs. Awake (n = 8). (***) means p < 0.001.

3.4. External Physical Stimuli Alter AuNP Migration and Biodistribution via the LA Interstitium

To investigate the regulatory effects of physical stimuli on nanoparticle transport through the LA interstitium, we compared AuNP migration characteristics and tissue distribution following electroacupuncture and moxibustion interventions (Figure 5). Micro-CT imaging revealed that, compared with the Anesthesia group, both the EA and Moxi groups exhibited enhanced longitudinal distribution of AuNPs along the LA interstitium (Figure 5A). Quantitative analysis demonstrated that AuNP migration trajectory length was significantly increased in both the EA and Moxi groups (** p < 0.01, Figure 5B). ICP-MS analysis revealed differences in tissue Au distribution among the Anesthesia, EA, and Moxi groups (Figure 5C). Mixed-effects model analysis showed a significant main effect of organ ($F(1.988, 41.74) = 13.90$, $p < 0.0001$) and a significant organ × treatment interaction ($F(16, 168) = 2.074$, $p = 0.0115$), whereas the main effect of treatment was not significant ($F(2, 21) = 0.7642$, $p = 0.4782$). In post hoc comparisons with the Anesthesia group, the EA group exhibited significantly elevated Au content in the heart (** p < 0.01), liver (* p < 0.05), lungs (* p < 0.05), uterus (*** p < 0.001), and blood (** p < 0.01); whereas the Moxi group showed significantly increased Au content only in the blood (** p < 0.01). Organ-to-liver Au content ratios were further compared among the Anesthesia, EA, Moxi, Awake, and Ctrl groups. Significant group differences were observed in the bladder-to-liver, ovary-to-liver, and uterus-to-liver ratios (* p < 0.05, ** p < 0.01, **** p < 0.0001, Figure 5D). Collectively, these findings suggest that electroacupuncture and

moxibustion interventions can differentially modulate the migration characteristics and tissue distribution of AuNPs following LA interstitial injection.

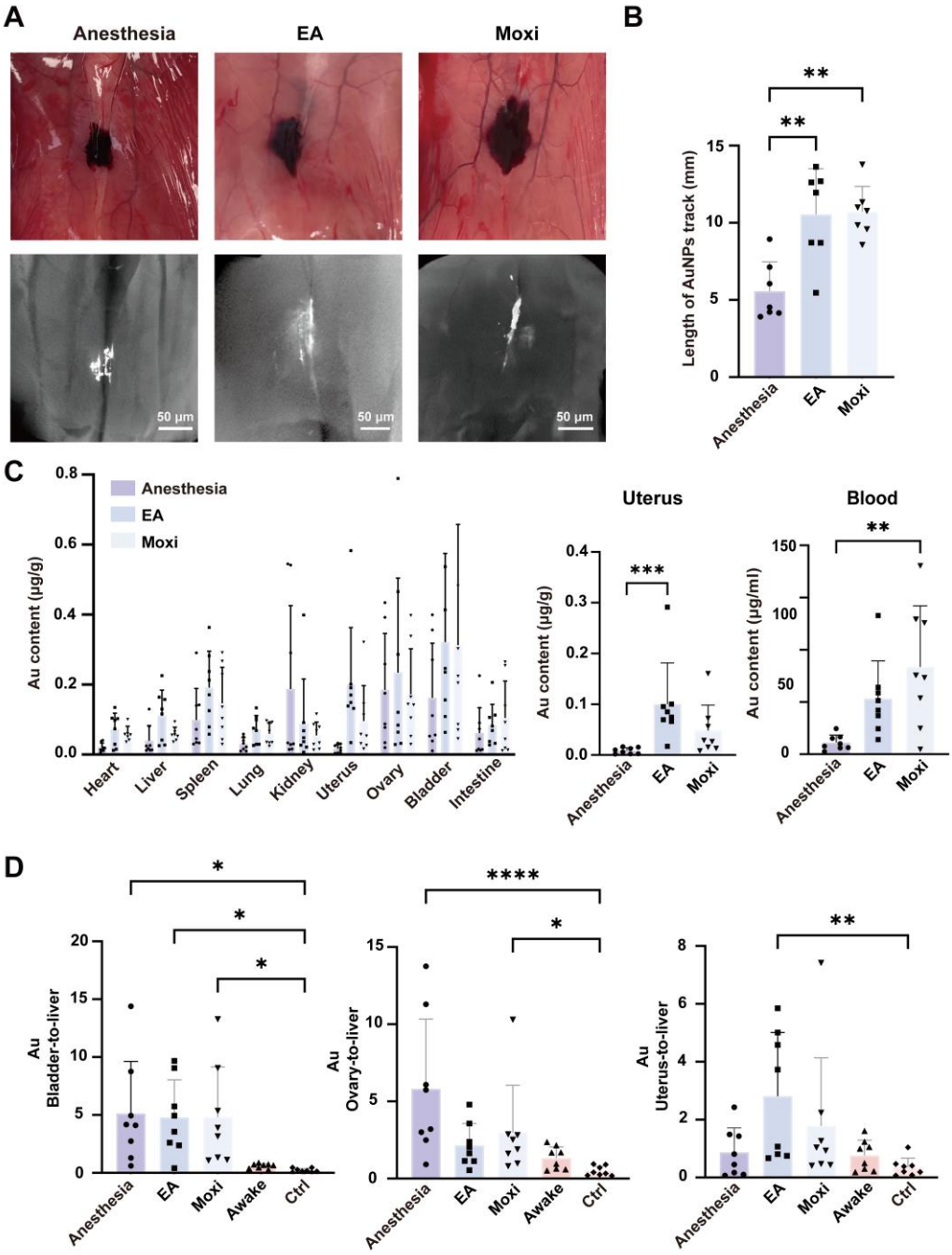


Figure 5. Physical stimulation regulates AuNP transport and biodistribution. (**A**) Micro-CT images of AuNP migration, Scale bar: 50 μm; (**B**) migration length of AuNPs, group-to-group comparisons ($n = 7$); (**C**) ICP-MS analysis of Au content in major organs and blood, group-to-group comparisons ($n = 8$); (**D**) organ-to-liver Au content ratios, group-to-group comparisons ($n = 8$). (*) means $p < 0.05$; (**) means $p < 0.01$; (***) means $p < 0.001$; (****) means $p < 0.0001$.

3.5. Structural Characteristics of the LA Interstitium

To characterize the structural features potentially relevant to interstitial transport in the LA interstitium, Masson's trichrome and immunofluorescence staining were performed. Compared with the adjacent paramedian connective tissue, the LA exhibited a distinctive interstitial architecture characterized by a continuous, relatively loose

reticular network of collagen fibers, with enlarged interfibrillar spaces and diverse fiber orientations. In contrast, the adjacent connective tissue showed more densely packed and predominantly parallel collagen bundles with narrower interstitial spaces. Col-I immunofluorescence staining further supported the presence of a relatively loose collagen framework in the LA. Moreover, immunofluorescence staining for CD31 and LYVE-1 showed a large number of lymphatic capillaries and a small number of capillaries distributed in the interstitial tissue of LA (Figure 6).

The porous loose connective tissue scaffold with ample space provides a low flow resistance dynamic condition for the flow of free interstitial fluid [20]. This may underpin the long-distance transport of Au through the LA. However, the present histological findings characterize tissue architecture and do not establish a causal relationship between collagen organization and nanoparticle migration. The respective contributions of collagen organization, interstitial fluid dynamics, and the associated microvascular and lymphatic structures remain to be determined.

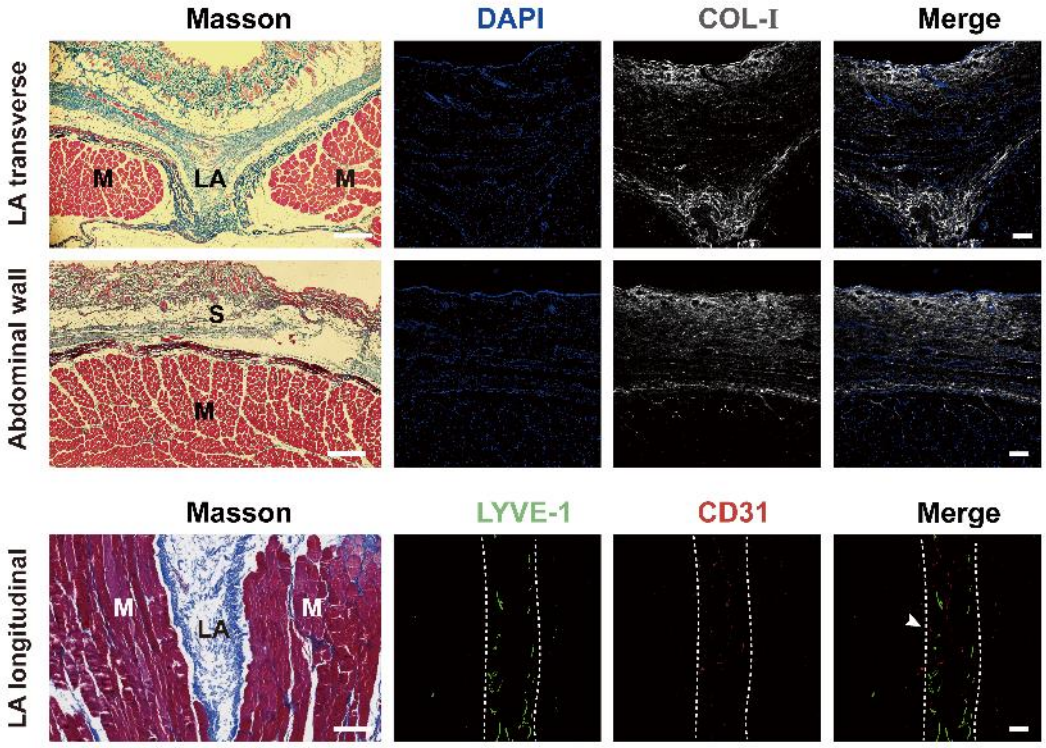


Figure 6. Structural characterization of the LA. Representative Masson staining and immunofluorescence images of COL-I in transverse LA and adjacent abdominal wall sections, and LYVE-1 and CD31 in longitudinal LA sections (n = 3). In the longitudinal LA sections, the white arrow and the white dashed lines indicate the LA region. COL-I, white; CD31, red; LYVE-1, green; DAPI, blue. S, skin; M, muscle. Scale bars: 500 μm for Masson staining and 100 μm for immunofluorescence staining.

4. Discussion

The interstitium is no longer regarded as a mere passive structural scaffold; rather, it is increasingly recognized as a dynamic transport microenvironment composed of ECM, collagen, and elastic fiber networks, hyaluronan, proteoglycans, and interstitial fluid [25,26]. A recent study indicated that interstitial spaces mediate local substance exchange and the long-distance transport of macromolecules and nanomaterials in tissues [18,27–29]. In the present study, AuNPs exhibited directional migration along the LA interstitium and a distinct early biodistribution profile, with relatively high normalized concentration-

based index values in selected pelvic organs. Notably, however, the comparable migration trajectory lengths between the Anesthesia and Ctrl groups were not associated with matching biodistribution profiles. This apparent dissociation may arise because trajectory length quantifies the macroscopic spatial extent of particle migration, while subsequent blood and organ distribution can be shaped by microscopic tissue architecture, local diffusion, and the relative contributions of interstitial and vascular transport. Thus, trajectory length alone may not fully capture the route-dependent distribution behavior of AuNPs, and the Micro-CT and ICP-MS findings should be considered complementary measures of nanoparticle distribution. Furthermore, histological examination further revealed that the LA interstitium possesses a continuous reticular collagen framework and enlarged interstitial spaces, features that are conspicuously absent in the adjacent paramedian connective tissue. This distinctive structural organization may contribute to the directional particle migration observed along the LA axis. The loosely woven collagen framework and enlarged interstitial spaces may influence local transport properties, although their specific effects on hydraulic resistance and convective transport remain to be determined. These structural features provide an anatomical basis for further investigating the role of the LA interstitium in nanoparticle transport.

The biodistribution profile resulting from LA interstitial administration differed strikingly from that achieved via intravenous injection. Following intravenous administration, Au predominantly accumulated in the liver, spleen, and lungs—organs that constitute the RES and are characterized by high blood perfusion and abundant phagocytic cell populations. The liver, as the largest metabolic and immunoregulatory organ, possesses a rich sinusoidal architecture replete with Kupffer cells that efficiently recognize and sequester circulating foreign nanoparticles through phagocytic and endocytic pathways [30–32]. Similarly, the spleen's open circulatory structure and its immune microenvironment—comprising macrophages, dendritic cells, and lymphocytes—enable continuous surveillance and clearance of blood-borne particulates, promoting pronounced nanoparticle entrapment [5,33]. The lungs, with their high blood flow, extensive capillary networks, and complex alveolar epithelial–macrophage interfaces, also represent a major sequestration site during the first pass of the pulmonary circulation [6]. After LA interstitial administration, the ovaries (23.04%) and bladder (20.22%) showed the highest normalized concentration-based index values. These findings are consistent with a contribution of interstitial migration along the LA pathway to the observed distribution pattern, although the relative contributions of interstitial transport, lymphatic drainage, and entry into the systemic circulation remain unresolved. LA interstitial administration was associated with a distinct early biodistribution profile compared with intravenous administration, although the underlying mechanisms remain unclear. Furthermore, the temporal dynamics and relative contributions of interstitial and systemic transport require further investigation.

Physiological state emerged as a significant modulator of LA-mediated nanoparticle distribution. Under awake, ambulatory conditions, Au exhibited enhanced systemic distribution compared with the anesthetized resting state, as evidenced by significantly increased blood gold concentrations and concomitant splenic accumulation. One possible explanation: rhythmic skeletal muscle contractions during voluntary movement augment interstitial fluid–lymphatic coupling, driving convective migration of nanoparticle-laden interstitial fluid toward lymphatic collectors and ultimately into the systemic circulation. In contrast, despite diminished systemic distribution of Au under anesthesia, pelvic organs, including the ovaries and bladder, exhibited markedly enhanced Au accumulation. One possible explanation is that anesthesia-related changes in interstitial fluid movement or lymphatic drainage may contribute to the observed distribution pattern. However, lymphatic transport and local Au retention were not directly quantified

in this study. The presence of lymphatic capillaries and relatively sparse blood capillaries in the LA provides anatomical context for possible lymphatic involvement in AuNP transport, but does not establish changes in lymphatic drainage under anesthesia. Such alterations may reroute the dominant transport pathway of AuNPs from systemic circulation to interstitial diffusion toward the pelvic region [34]. These findings suggest that maintenance of a relatively quiescent state during the early period after LA interstitial injection coincides with accumulation of nanoparticles in pelvic organs, whereas increased physical activity is accompanied by their entry into the systemic circulation. Collectively, these observations underscore that nanoparticle delivery strategies based on endogenous interstitial networks must account for the dynamic equilibrium among administration conditions, interstitial migration kinetics, and circulatory clearance—a consideration that carries important implications for developing novel nano-delivery approaches tailored to pelvic and deep-seated organ diseases.

Both electroacupuncture and moxibustion interventions significantly increased AuNP migration along the LA interstitium; however, they produced distinct distribution patterns. Electroacupuncture intervention was associated with a particularly pronounced increase in Au accumulation in the uterus, while Au levels were also slightly increased in several systemic organs, including the heart, liver, and lungs. The elevated AuNP accumulation in non-pelvic organs may reflect the combined effects of electroacupuncture intervention on local interstitial transport and systemic circulatory distribution. Mechanical stimulation, such as that generated by acupuncture needle manipulation, has been shown to alter ECM tension and interstitial fluid dynamics; periodic mechanical deformation can contribute to a "gel pump"-like effect within the interstitial matrix, potentially facilitating long-range convection of interstitial fluid and associated solutes [35]. Additionally, local mechanical stimulation may modulate ECM mechanical properties and tissue-level mechanotransduction signaling [36]. We hypothesize that electroacupuncture may influence AuNP transport toward pelvic structures, particularly the uterus, by modulating local interstitial fluid dynamics and matrix–fluid coupling, while also increasing systemic availability of a fraction of the transported AuNPs, although their relative contributions remain unresolved. However, moxibustion produced a more pronounced increase in circulating Au levels, whereas its effect on pelvic organ accumulation was comparatively limited. Previous studies have shown that thermal stimulation can promote vasodilation, increase local blood perfusion, and enhance microcirculatory exchange; elevated temperature may also reduce interstitial fluid viscosity and alter matrix permeability, thereby potentially influencing local solute transport [37]. These thermal effects are consistent with the increased circulating Au levels observed after moxibustion in the present study. However, nanoparticle accumulation at the organ level is influenced by multiple factors, including circulating AuNP levels, organ perfusion, vascular permeability, tissue uptake, post-administration time, and clearance. Thus, the comparatively limited increase in organ accumulation despite elevated circulating Au levels may reflect inter-organ differences in these tissue-specific determinants. Accordingly, the distribution pattern associated with moxibustion may indicate a greater contribution of vascular–circulatory processes to systemic Au exposure, although the relative contributions of these processes to tissue distribution remain unresolved. Taken together, these findings suggest that physical stimuli may modulate LA-associated nanoparticle distribution, with electroacupuncture associated with uterine accumulation and moxibustion with systemic transport.

The present study provides proof-of-concept evidence that the LA interstitium can support nanoparticle migration and is associated with distinct early biodistribution patterns that vary with physiological state and physical stimulation. These findings broaden the investigation of nanoparticle delivery beyond vascular administration by

highlighting the potential of endogenous interstitial architecture to influence early organ-level biodistribution. However, several limitations warrant acknowledgment. First, our biodistribution assessments were conducted at a single acute time point (20 or 30 min post-injection); the long-term retention, clearance kinetics, and potential degradation of AuNPs delivered via this route remain to be characterized. Additionally, the injection volumes differed between the LA and i.v. groups (25 vs. 30 μL), and potential tail retention during i.v. injection was not quantified, leaving uncertainty about the actual dose entering systemic circulation despite normalization to %ID/g. Second, although we have established the structural correlates of LA transport, the precise molecular mediators, including specific ECM components, adhesion molecules, or channel-forming proteins, that govern particle movement within this interstitium have not been elucidated. Third, this study describes only the delivery profile of AuNPs in the LA interstitium and does not evaluate their therapeutic utility, long-term safety, clearance kinetics, or the delivery of an active drug payload. Future studies should integrate real-time dynamic imaging techniques with functional nanocarrier systems to delineate the spatiotemporal dynamics and therapeutic applicability of LA-mediated delivery. As the transport characteristics and regulatory mechanisms of the LA interstitium become increasingly clear, this endogenous structural network may emerge as a valuable platform for developing next-generation precision nano-delivery strategies.

5. Conclusions

This study provides evidence that the LA interstitium supports directional, relatively long-range nanoparticle delivery and is associated with a distinct early biodistribution pattern. Following LA administration, Au levels showed normalized concentration-based index values of 23.04% in the ovaries and 20.22% in the bladder, compared with predominant accumulation in the spleen (36.76%), liver (18.20%), and lungs (15.03%) after intravenous administration. LA administration also increased Au content in the ovaries and bladder compared with paramedian muscle injection. AuNP delivery were modulated by physiological state and physical stimulation: the awake state increased migration length and blood Au levels, whereas anesthesia was associated with relatively greater pelvic distribution; electroacupuncture enhanced uterine Au accumulation, while moxibustion predominantly increased circulating Au levels. Collectively, these findings support the potential of the LA interstitium for nanoparticle transport and highlight its modulation by physiological and physical conditions. As AuNPs were used solely as tracers, this study provides preliminary proof of concept but does not establish delivery efficacy or therapeutic benefit. Future studies should evaluate drug-loaded nanocarriers for delivery efficiency, long-term biodistribution, clearance, and biosafety, which were not assessed in the present study.

Supplementary Materials: The following supporting information can be downloaded at https://www.mdpi.com/article/10.3390/biomedicines14112534/s1. Table S1. Hydrodynamic diameter, polydispersity index (PDI), and zeta potential of the same AuNPs suspension monitored over a 6-day storage period. Data are presented as mean ± SD.

Author Contributions: Conceptualization, W.Z., R.H., X.S. and Y.J.; methodology, X.S. and Y.J.; software, Y.J. and Y.S.; validation, X.S. and Y.J.; formal analysis, G.W. and S.Z.; investigation, S.W., Y.A., J.L. and Y.J.; resources, G.W. and S.J.; data curation, Y.S. and Y.L.; writing—original draft preparation, Y.J.; writing—review and editing, R.H. and X.S.; visualization, Y.J.; supervision, R.H. and X.S.; project administration, R.H. and X.S.; funding acquisition, G.W., R.H. and X.S. All authors have read and agreed to the published version of the manuscript.

Funding: This research was supported by the National Key Research and Development Program of China (Grant No. 2024 YFA1209901, No.2024 YFA1209903, No. 2024 YFA1209904) and Beijing Municipal Science & Technology Commission, Administrative Commission of Zhongguancun Science Park project (Grant No. Z251100006925031).

Institutional Review Board Statement: The animal study protocol was approved by the Animal Ethics Committee of the Institute of Acupuncture and Moxibustion, China Academy of Chinese Medical Sciences (Approval No.: D2023-01-10-01; Date: 10 January 2023).

Informed Consent Statement: Not applicable.

Data Availability Statement: The data presented in this study are available upon request from the corresponding authors. Due to ethical considerations, these data are not publicly available.

Acknowledgments: The researchers would like to thank Yu Wang from the Institute of Genetics and Developmental Biology, Chinese Academy of Sciences, for his valuable technical support and assistance with Micro-CT imaging and analysis. We are also particularly grateful to Lu Huang from the Institute of Genetics and Developmental Biology, Chinese Academy of Sciences, for funding support for this project from the Beijing Municipal Science & Technology Commission and the Administrative Commission of Zhongguancun Science Park project (Grant No. Z251100006925031).

Conflicts of Interest: The authors declare no conflicts of interest.

Abbreviations

The following abbreviations are used in this manuscript:

AuNPs	Gold nanoparticles
LA	Linea alba
PEG	Polyethylene glycol
EA	Electroacupuncture
Moxi	Moxibustion
i.v.	Intravenous injection
ICP-MS	Inductively coupled plasma mass spectrometry
COL-I	type I collagen
LYVE-1	Lymphatic vessel endothelial hyaluronan receptor 1
CD31	Platelet endothelial cell adhesion molecule-1

References

1. Patra, J.K.; Das, G.; Fraceto, L.F.; Campos, E.V.R.; Rodriguez-Torres, M.D.P.; Acosta-Torres, L.S.; Diaz-Torres, L.A.; Grillo, R.; Swamy, M.K.; Sharma, S.; et al. Nano-Based Drug Delivery Systems: Recent Developments and Future Prospects. *J. Nanobiotechnol.* **2018**, *16*, 71.
2. Skotland, T.; Iversen, T.G.; Llorente, A.; Sandvig, K. Biodistribution, Pharmacokinetics and Excretion Studies of Intravenously Injected Nanoparticles and Extracellular Vesicles: Possibilities and Challenges. *Adv. Drug Deliv. Rev.* **2022**, *186*, 114326.
3. Corbo, C.; Molinaro, R.; Parodi, A.; Toledano Furman, N.E.; Salvatore, F.; Tasciotti, E. The Impact of Nanoparticle Protein Corona on Cytotoxicity, Immunotoxicity and Target Drug Delivery. *Nanomedicine* **2016**, *11*, 81–100.
4. Shao, Q.; Ding, T.; Pan, F.; Li, G.; Shen, S.; Qian, J.; Zhan, C.; Wei, X. Protein Corona Mediated Liposomal Drug Delivery for Bacterial Infection Management. *Asian J. Pharm. Sci.* **2022**, *17*, 855–866.
5. Cabral, H.; Li, J.; Miyata, K.; Kataoka, K. Controlling the biodistribution and clearance of nanomedicines. *Nat. Rev. Bioeng.* **2024**, *2*, 214–232.
6. Kozics, K.; Sramkova, M.; Kopecka, K.; Begerova, P.; Manova, A.; Krivosikova, Z.; Sevcikova, Z.; Liskova, A.; Rollerova, E.; Dubaj, T.; et al. Pharmacokinetics, Biodistribution, and Biosafety of PEGylated Gold Nanoparticles In Vivo. *Nanomaterials* **2021**, *11*, 1702.
7. De, T.; Trieu, V.; Myers, S.; Qazi, S.; Saund, S.; Lee, C. Sub-15 nm Nanoparticles for Drug Delivery: Emerging Frontiers and Therapeutic Potential. *Int. J. Mol. Sci.* **2025**, *26*, 10842.

8. Zhuang, J.; Zhang, X.; Liu, Q.; Zhu, M.; Huang, X. Targeted Delivery of Nanomedicines for Promoting Vascular Regeneration in Ischemic Diseases. *Theranostics* **2022**, *12*, 6223–6241.
9. Chen, H.; Wang, L.; Zeng, X.; Schwarz, H.; Nanda, H.S.; Peng, X.; Zhou, Y. Exosomes, a New Star for Targeted Delivery. *Front. Cell Dev. Biol.* **2021**, *9*, 751079.
10. Barua, S.; Mitragotri, S. Challenges Associated with Penetration of Nanoparticles across Cell and Tissue Barriers: A Review of Current Status and Future Prospects. *Nano Today* **2014**, *9*, 223–243.
11. Netti, P.A.; Berk, D.A.; Swartz, M.A.; Grodzinsky, A.J.; Jain, R.K. Role of Extracellular Matrix Assembly in Interstitial Transport in Solid Tumors. *Cancer Res.* **2000**, *60*, 2497–2503.
12. Stylianopoulos, T.; Wong, C.; Bawendi, M.G.; Jain, R.K.; Fukumura, D. Chapter Six—Multistage Nanoparticles for Improved Delivery into Tumor Tissue. In *Methods in Enzymology*; Düzgüneş, N., Ed.; Academic Press: Cambridge, MA, USA, 2012; Volume 508, pp. 109–130.
13. Sriraman, S.K.; Aryasomayajula, B.; Torchilin, V.P. Barriers to Drug Delivery in Solid Tumors. *Tissue Barriers* **2014**, *2*, e29528.
14. Li, H.; Song, F.; Hu, X.; Jing, L.; Shuai, Q.; Su, W.; Pich, A.; Li, X. Tailored Nanogel Network Topology Enables Clinical Ultrasound-Induced Mechanochemical Activation for In Vivo Therapy. *Angew. Chem. Int. Ed*. **2026**, *65*, e4591365.
15. Li, H.; Yin, Y.; Yang, C.; Chen, M.; Wang, F.; Ma, C.; Li, H.; Kong, Y.; Ji, F.; Hu, J. Active Interfacial Dynamic Transport of Fluid in a Network of Fibrous Connective Tissues throughout the Whole Body. *Cell Prolif.* **2020**, *53*, e12760.
16. Li, H.Y. Verification and Challenges of Interstitial Fluid Circulatory Network. *Chin. J. Front. Med. Sci. (Electr. Vers.)* **2023**, *15*, 75–80.
17. Sun, W.; Zhang, X.; Zhao, Y.; Ye, B.; Gao, W.; Jiang, G.; Li, X.; Lin, X. pH/NIR Dual-Responsive Implantable Patch for Combined Photothermal and Chemotherapy of Tumors. *Int. J. Pharm. X* **2026**, *11*, 100582.
18. Zhang, X.; Sun, W.; Li, X.; Li, Y.; Xiang, S.; Zhang, L.; Yang, Y. Cyano-Modulated Zn(II)-Schiff Base Complexes for Lysosome-Targeted Fluorescence Imaging and pH-Responsive Camptothecin Delivery. *Int. J. Pharm. X* **2026**, *12*, 100594.
19. Benias, P.C.; Wells, R.G.; Sackey-Aboagye, B.; Klavan, H.; Reidy, J.; Buonocore, D.; Miranda, M.; Kornacki, S.; Wayne, M.; Carr-Locke, D.L.; et al. Structure and Distribution of an Unrecognized Interstitium in Human Tissues. *Sci. Rep.* **2018**, *8*, 4947.
20. Song, X.; Zhang, W.; Jia, S.; Wang, G.; Wang, S.; Li, H.; Xiong, F. A Discovery of Low Hydraulic Resistance Channels along Meridians in Rats. *World J. Acupunct. Moxibustion* **2021**, *31*, 22–29.
21. Zhu, Y.; Lu, G.; Li, W.; Su, C.; Du, P.; Wang, S.; Yang, L.; Xu, H.; Fang, Y.; Song, X. Interstitial Fluid Transport in Linea Alba Is Involved in Acupuncture-Induced Attenuation of Ovarian Hypofunction in Aged Rats. *Front. Endocrinol.* **2025**, *16*, 1579031.
22. Zhang, Z.; Huang, H.; Yue, J.; Zhu, X.; Shi, Y.; Shen, B.; Zhu, Q.; Mei, L.; Chen, Q. Ptgs2+ CPTC Function as a "Force-Immune Axis" by Responding to Acupuncture and Mediating M2 Macrophage Activation for Anti-Inflammatory Effects. *FASEB J.* **2025**, *39*, e71048.
23. Jia, S.; Wang, Q.; Li, H.; Song, X.; Wang, S.; Zhang, W.; Wang, G. Pilot Study of Blood Perfusion Changes at PC4 and Its Surrounding Points Induced by Acupuncture and Moxibustion. *Evid. Based Complement. Alternat. Med.* **2021**, *2021*, 2431570.
24. Turkevich, J.; Stevenson, P.C.; Hillier, J. A Study of the Nucleation and Growth Processes in the Synthesis of Colloidal Gold. *Discuss. Faraday Soc.* **1951**, *11*, 55–75.
25. Cenaj, O.; Allison, D.H.R.; Imam, R.; Zeck, B.; Drohan, L.M.; Chiriboga, L.; Llewellyn, J.; Liu, C.Z.; Park, Y.N.; Wells, R.G.; et al. Evidence for Continuity of Interstitial Spaces across Tissue and Organ Boundaries in Humans. *Commun. Biol.* **2021**, *4*, 436.
26. Liu, W.T.; Cao, Y.P.; Zhou, X.H.; Han, D. Interstitial Fluid Behavior and Diseases. *Adv. Sci.* **2022**, *9*, e2100617.
27. Stewart, R.H. A Modern View of the Interstitial Space in Health and Disease. *Front. Vet. Sci.* **2020**, *7*, 609583.
28. Shi, Y.; Jiao, C.; Lu, X.; Nie, Y.; Li, X.; Han, D. Rapamycin Nanoparticles Improves Drug Bioavailability in PLAM Treatment by Interstitial Injection. *Orphanet J. Rare Dis*. **2022**, *17*, 349.
29. Sariano, P.A.; Mizenko, R.R.; Shirure, V.S.; Brandt, A.K.; Nguyen, B.B.; Nesiri, C.; Shergill, B.S.; Brostoff, T.; Rocke, D.M.; Borowsky, A.D.; et al. Convection and extracellular matrix binding control interstitial transport of extracellular vesicles. *J. Extracell. Vesicles* **2023**, *12*, e12323.
30. Sadauskas, E.; Wallin, H.; Stoltenberg, M.; Vogel, U.; Doering, P.; Larsen, A.; Danscher, G. Kupffer Cells Are Central in the Removal of Nanoparticles from the Organism. *Part. Fibre Toxicol.* **2007**, *4*, 10.
31. Jiang, K.; Tian, K.; Yu, Y.; Wu, E.; Yang, M.; Pan, F.; Qian, J.; Zhan, C. Kupffer Cells Determine Intrahepatic Traffic of PEGylated Liposomal Doxorubicin. *Nat. Commun.* **2024**, *15*, 6136.
32. Sibuyi, N.R.S.; Moabelo, K.L.; Fadaka, A.O.; Meyer, S.; Onani, M.O.; Madiehe, A.M.; Meyer, M. Multifunctional Gold Nanoparticles for Improved Diagnostic and Therapeutic Applications: A Review. *Nanoscale Res. Lett.* **2021**, *16*, 174.

33. Tian, X.; Yuan, Y. Impacts of Polyethylene Glycol (PEG) Dispersity on Protein Adsorption, Pharmacokinetics, and Biodistribution of PEGylated Gold Nanoparticles. *RSC Adv.* **2024**, *14*, 20757–20764.
34. Dull, R.O.; Hahn, R.G. Hypovolemia with peripheral edema: What is wrong? *Crit. Care* **2023**, *27*, 206.
35. Li, H.Y.; Wang, F.; Chen, M.; Zheng, Z.J.; Yin, Y.J.; Hu, J.; Li, H.; Sammer, A.; Feigl, G.; Maurer, N.; et al. An Acupoint-Originated Human Interstitial Fluid Circulatory Network. *Chin. Med. J.* **2021**, *134*, 2365–2369.
36. Langevin, H.M.; Bouffard, N.A.; Churchill, D.L.; Badger, G.J. Connective Tissue Fibroblast Response to Acupuncture: Dose-Dependent Effect of Bidirectional Needle Rotation. *J. Altern. Complement. Med.* **2007**, *13*, 355–360.
37. Huang, C.; Sheu, T.W.H. Study of the Effect of Moxibustion on the Blood Flow. *Int. J. Heat Mass Transf.* **2013**, *63*, 141–149.

Disclaimer/Publisher's Note: The statements, opinions and data contained in all publications are solely those of the individual author(s) and contributor(s) and not of MDPI and/or the editor(s). MDPI and/or the editor(s) disclaim responsibility for any injury to people or property resulting from any ideas, methods, instructions or products referred to in the content.